JOURNAL OF GUIDANCE, CONTROL, AND DYNAMICS
Vol. 32, No. 6, November–December 2009

In-Flight Trajectory Planning and Guidance for Autonomous Parafoils

Branden J. Rademacher* and Ping Lu†
Iowa State University, Ames, Iowa 50011-2271
and
Alan L. Strahan‡ and Christopher J. Cerimele§
NASA Johnson Space Center, Houston, Texas 77058

DOI: 10.2514/1.44862

This paper presents a framework for onboard trajectory planning and guidance for a large class of autonomously guided parafoils. The problem is for the parafoil to reach a given location at a specified altitude with a specified final heading. Through appropriate change of the independent variable, the trajectory planning problem is converted from a three-dimensional free-final-time problem to a two-dimensional fixed-final-time problem. Using the well-known Dubins path synthesis and known parafoil performance parameters, a concept of altitude margin is developed as a quantitative measure of the available maneuvering energy for use in trajectory planning. A hybrid strategy using two methods to generate kinematically feasible fixed-time trajectories is presented, each targeting a different range of initial values of the altitude margin. The trajectory can be replanned onboard in every guidance cycle, making the guidance effectively closed-loop, or replanned whenever the actual deviation of the actual condition from the reference trajectory exceeds a threshold. The proposed planning and guidance algorithm applies to a large class of parafoil canopies and payloads, which encompasses wide variations in the lift-to-drag ratio, wing loading, and maximum turn rate. The guidance logic has the potential of requiring little or no tuning to accommodate variations in canopy performance. Monte Carlo simulations are conducted to evaluate the effectiveness of the algorithm with dispersions in canopy performance, loading, wind profile errors, navigation uncertainty, using lateral control only, and using both longitudinal and lateral control.

I. Introduction

AUTONOMOUSLY guided parafoils have many applications including precision airdrop, weapons delivery, remote sensor placement, spacecraft landing, and planetary exploration. Gliding parachutes offer a number of advantages over conventional parachutes including the ability to penetrate wind to reduce landing errors and the ability to deploy the system a significant distance from the target.

The parafoil guidance problem is to generate a trajectory from a given initial configuration (position and heading) (x_0, y_0, ψ_0) at some altitude h_0 to a given a terminal position (x_f, y_f) or configuration (x_f, y_f, ψ_f) at some specified final altitude h_f. There are many challenges facing any guidance algorithm for autonomous parafoils. Unlike powered vehicles, parafoils generally have no ability to ascend. This means that only one attempt can be made at landing. Most parafoil systems use yaw rate or yaw acceleration as the primary means of control and thus have little or no ability to reduce the along-track trajectory tracking error. Furthermore, the turn response and glide performance can vary greatly depending on canopy size and loading, which may change from mission to mission. Another significant complication is that the wind profile has a profound impact on the motion of the system and is often not known in advance or may only be known approximately. The wind velocity at certain altitudes may exceed the vehicle airspeed, meaning that during certain portions of the flight the system may not be able to make forward progress with respect to the ground. A good guidance algorithm must be robust to all of these adverse conditions. For a given canopy and loading, this is best accomplished by preserving maneuvering energy as long as possible in the trajectory.

There are many applications in which it is desired to minimize the impact force upon landing. This requirement conflicts with the requirement to minimize the landing dispersion resulting from uncertainty in the wind profile. Overcoming wind uncertainty is best accomplished with a higher canopy loading, which increases the system airspeed. The side effect is that both the horizontal and vertical airspeeds are higher, increasing the impact force. Some systems such as the Onyx by Atair Aerospace [1] or the Screamer by Strong Enterprises [2] overcome this problem by using a smaller, higher-loaded, parafoil canopy to track to the target and dissipate excess altitude and then release a secondary nongliding parachute over the target to achieve a soft landing. However, in certain missions the size of the parafoil or the extra weight of the secondary chute may not allow for this approach. In such instances, the alternative is to use a lower canopy loading and land with the vehicle airspeed vector pointed into the wind.

Several algorithms for parafoil guidance, navigation, and control (GNC) are found in the literature. The algorithms generate trajectories that typically fall into one of three categories. Waypoint-based algorithms [3,4] generate a sequence of waypoints to manage excess altitude and have various criteria for exiting the energy management phase and tracking to the target. Maneuver-based algorithms [1] generate a reference glide slope to the target, usually biased from the true system glide slope to allow for wind uncertainty, and perform a sequence of maneuvers to maintain the reference glide slope. Path-based algorithms [5–7] generate a continuous reference trajectory connecting the system position and orientation to the target, and the trajectory is usually parameterized by time or altitude. Other algorithms [8,9] may use a hybrid combination of these

Presented as Paper 7417 at the AIAA Guidance, Navigation, and Control Conference and Exhibit, Honolulu, HI, 18–21 August 2009; received 10 April 2009; accepted for publication 26 July 2009.

*Graduate Research Assistant, Department of Aerospace Engineering, 2271 Howe Hall, Room 1200. Student Member AIAA.
†Professor, Department of Aerospace Engineering, 2271 Howe Hall; plu@iastate.edu. Associate Fellow AIAA.
‡Aerospace Engineer, Mail Code EG4.
§Branch Chief, Flight Mechanics and Trajectory Design Branch, Mail Code EG5.

methods, typically one for energy management and one for final tracking to the target. Most algorithms conduct planning in the plane and remove the influence of the wind by working in a wind-fixed coordinate frame. Some algorithms can handle additional constraints placed on the trajectory, including the addition of specific geographic waypoints, obstacle or geographic area avoidance, and final heading constraints.

The algorithms that generate trajectories with a fixed final heading are typically tailored to a specific parafoil canopy and payload and would require modification to be applied to a different class of canopy and payload. For example, the algorithms in [5–7] assume that the glide-path angle and airspeed are constant during both straight-line and turning portions of the reference trajectory. This assumption works well for very large canopies that have little variation in airspeed and glide-path angle even at the maximum turning rate. Smaller canopies, however, can have significant variation in both quantities, and neglecting these variations in trajectory planning overestimates the glide performance of the system. As a second example, the algorithm in [3] generates a waypoint-based trajectory. The spacing of the waypoints and the tolerances for determining when a waypoint is considered to be reached need to be adjusted based on the minimum turn radius of the system, which is dependent on the canopy and loading. The resulting trajectory also contains a series of possibly alternating turns of large magnitude that may not be suitable for larger canopies with limited maximum turn rates. In general, the available GNC algorithms are best applied to a restricted class of parafoils with a limited range of canopy performance. What is generally lacking is a unified guidance approach that performs well for a large class of parafoils and is easily adaptable to gross variations in the lift-to-drag ratio L/D, wing loading W/S, and maximum turn rate/acceleration.

Parafoil dynamics are nonholonomic as instantaneous motion is constrained to be tangent to the velocity vector. There is a significant body of related research on nonholonomic path planning in the robotics community. The original work by Dubins [10] and subsequent work by Boissonnat et al. [11] discuss minimum-time paths connecting two configurations for carlike vehicles with constant forward velocity and maximum-turn-rate constraints. This type of vehicle is commonly referred to as the Dubins car, and the minimum-time paths are referred to as Dubins paths or Dubins curves. McGee et al. [12] apply the Dubins path approach to find trajectories for unmanned aerial vehicles operating in a constant wind field. McNeely et al. [13] generalize the result of McGee et al. [12] to include multiple waypoints in the trajectory. Larson et al. [14] use a Dubins path synthesis and dynamic programming to generate trajectories for unmanned aerial vehicles to reach the final configuration at a specified time. A three-dimensional extension to Dubins's work is given by Sussmann [15]. Liang et al. [16] generate curvature-bounded trajectories for Dubins carlike robots using cubic spirals. Moll [17] describes a method for finding minimal energy paths of constant length. Lu and Chavez [18] use an optimal control synthesis to generate minimum-control (turn rate) trajectories for both free- and fixed-final-heading cases in a free final time.

In this paper we consider the parafoil trajectory planning problem with the final configuration fixed. In Sec. II we develop a reduced-order parafoil model for trajectory planning and cast the three-dimensional path planning problem as a two-dimensional planning problem through a suitable change of the independent variable. In Sec. III we use an optimal control synthesis to solve the resulting boundary-value problem. Using the well-known Dubins path result for minimum-time trajectories we are able to define a parameter, the altitude margin, that is used by the guidance algorithm to determine if the specified final configuration is reachable and give a qualitative measure of the difficulty in reaching it. A necessary condition for the existence of a fixed-time path is also derived. We present a hybrid strategy to use two methods of generating general fixed-time trajectories, one targeting the cases of very low or very high altitude margin and the other for the rest of cases. In Sec. IV we present a simple baseline trajectory tracking controller. In Sec. V we present a closed-loop guidance algorithm that is parameterized directly on the parafoil canopy performance. In this way, the guidance logic can be easily applied to a large class of parafoil canopies and payloads. In Sec. VII we conduct Monte Carlo simulations to predict expected landing accuracy and determine the sensitivity of the proposed guidance algorithm to a number of potential disturbances. Monte Carlo simulations are performed using only lateral control and using both lateral and longitudinal glide slope control. The results indicate that a significant improvement in landing accuracy can be obtained when longitudinal control is available.

II. Parafoil and Environment Modeling

In this section we describe a low-fidelity dynamic model to represent macromotion of a parafoil for use in guidance and control design. Transient motion due to changes in the angle of attack tends to be small in magnitude and damps out quickly relative to the time required to change flap settings, due to inherent rate limitations in the winches used to affect control flap deflections. The model discussed herein applies to a wide range of parafoil canopies and payloads that encompass gross variations in canopy size, loading, aerodynamic performance, and maximum turn rate. The model captures all of the key behaviors particular to parafoil motion while requiring as few parameters as possible. The key macromotion behaviors of interest are that the glide-path angle and glide airspeed increase with turn rate. Apparent mass (discussed subsequently) terms do not explicitly show up in the model, though the primary effects resulting from apparent mass that are important for guidance design are sufficiently captured. Finally, the model readily lends itself to reduction and simplification for trajectory planning purposes. We follow the modeling approach in [1] with some subtle differences to add the capability for longitudinal control.

The parafoil canopy is a very light structure that is far removed from the center of mass of the parafoil/ payload system. As such, parafoil motion is strongly influenced by the so-called apparent mass effects of the surrounding air. The origins of this phenomenon are discussed in detail by Thomasson [19] and a method for approximating the apparent mass terms for parafoils is given by Barrows [20]. In this current work we are interested in two key behaviors arising from apparent mass effects. First, apparent mass tends to increase the skid common to parafoils that use asymmetrical trailing-edge deflections for turn control. Depending on the size of the canopy, the bank angle can be significantly less than the bank angle for a coordinated turn. This disparity becomes larger as the canopy area becomes larger. Second, apparent mass has a profound impact on the sensitivity of a given canopy to control input. Small, highly loaded canopies tend to be extremely sensitive, and large canopies can have an overly sluggish response [21].

Parafoil control is most commonly affected by deflection of flaps, which are defined as the outer quarters of the trailing edge of the canopy. Lateral control is achieved by an asymmetric deflection of the flaps that directly induce yaw rate rather than roll rate. Longitudinal control is achieved by a symmetric flap deflection and the effect depends on the specific canopy, the magnitude of the symmetric deflection, and the rigging angle of the canopy, which is defined in Fig. 1. For moderate rigging angles, moderate symmetric flap deflections produce an increase in the lift force and a corresponding increase in the drag force. The result is a decrease in glide velocity but little change in glide-path angle, as L/D remains roughly constant. However, aerodynamic data from [22,23] indicate that at shallower rigging angles and larger symmetric flap deflections, appreciable changes in the flight-path angle can be made. Data from these sources also suggest that altering the rigging angle in flight can appreciably change the flight-path angle. However, great care must be used in implementing such a scheme, as incorrect rigging can lead to stall onset, leading-edge collapse, unintentional retrimming at multiple angles of attack, and loss of lateral stability [24]. In the model described in the sequel, provision is made for both forms of longitudinal control.

A. Parafoil Equations of Motion

Consider the fore view of the traditional wind frame of a parafoil in turning flight, shown on the left side of Fig. 2. Here, L is the sum of

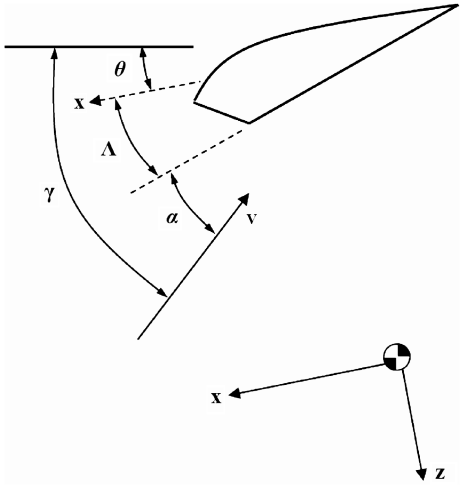

Fig. 1 The relationship between the angle of attack α, the pitch angle θ, the flight-path angle γ, and the rigging angle Λ. (Note that γ and θ are negative as shown.)

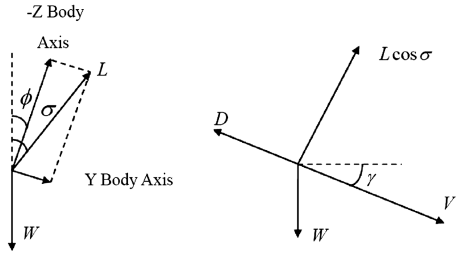

Fig. 2 Force diagram for a parafoil in turning flight: fore view (left) and side view (right).

the aerodynamic forces perpendicular to the velocity vector, W is the weight force vector, ϕ is the true bank angle, and σ can be thought of as the bank angle of L. Note that the velocity and drag force vector components are omitted for clarity, and L as shown is the vertical projection of the true force onto the page.

The side view is shown on the right side of Fig. 2. Here, V is the airspeed velocity vector, D is the vector sum the aerodynamic forces parallel to the airspeed vector, and γ is the flight-path angle (negative as shown). The equations of motion for a parafoil over a flat, nonrotating Earth in a locally constant wind field can be written as

$$\dot{V} = -\frac{(D + W\sin\gamma)}{m} \tag{1}$$

$$\dot{\gamma} = \frac{(L\cos\sigma - W\cos\gamma)}{mV} \tag{2}$$

$$\dot{\psi} = \frac{L\sin\sigma}{mV\cos\gamma} \tag{3}$$

$$\dot{x} = V\cos\gamma\cos\psi + w_x \tag{4}$$

$$\dot{y} = V\cos\gamma\sin\psi + w_y \tag{5}$$

$$\dot{h} = V\sin\gamma \tag{6}$$

$$\dot{\sigma} = (\sigma_{\text{com}} - \sigma)/\tau_\sigma \tag{7}$$

$$\dot{\varepsilon} = (\varepsilon_{\text{com}} - \varepsilon)/\tau_\varepsilon \tag{8}$$

where ψ is the azimuth angle of the velocity vector, x is the downrange distance, y is the cross-range distance, h is the altitude above the ground, σ is the pseudo bank angle, ε is a parameter that affects the lift and drag forces, W is the weight of the system (including the payload and the canopy), and w_x and w_y are the x and y components of the wind at the current position and altitude. The coordinate frame is chosen such that the origin coincides with the target at $h = 0$ with the x axis in the ground plane *pointing into* the assumed wind at $h = 0$. The y axis is rotated 90 deg clockwise and also in the ground plane. The z axis completes the right-handed coordinate frame so that $h = -z$. In addition, limits on $\dot{\psi}$, $\dot{\sigma}$, and $\dot{\varepsilon}$ are enforced. The lift and drag forces are modeled as

$$L = 0.5\rho V^2 S(C_{L_{\text{trim}}} + \delta C_L(\varepsilon)) \tag{9}$$

$$D = 0.5\rho V^2 S(C_{D_{\text{trim}}} + \delta C_D(\varepsilon)) \tag{10}$$

where ρ is the density of the air and a function of altitude, S is the canopy area, and $C_L = C_{L_{\text{trim}}} + \delta C_L$ and $C_D = C_{D_{\text{trim}}} + \delta C_D$ are the lift and drag coefficients, respectively. Variations in ε represent the effects of altering the symmetric flap defection and/or the canopy rigging angle, and they produce increments δC_L and δC_D. It is assumed that for $\varepsilon = 0$, $\delta C_L = 0$ and $\delta C_D = 0$, and thus C_L and C_D take on their trim values $C_{L_{\text{trim}}}$ and $C_{D_{\text{trim}}}$.

There are two control inputs for this model. The first is σ_{com}, which is essentially a commanded turn rate and represents an asymmetric flap deflection. The second control input is ε_{com}, which represents the commanded change in the longitudinal control (either a symmetric flap deflection or change of the rigging angle) and is essentially a commanded glide-path angle.

B. Reduced-Order Model

For trajectory planning purposes, a further simplified model is required to reduce computational burden and aid analysis. To simplify the model in the preceding section, we begin by enforcing a quasi-equilibrium-glide assumption and then change the independent variable from time to a function of altitude. These changes reduce the system order and simplify the trajectory planning problem. The final step in simplifying the model is converting to a wind-fixed coordinate frame to remove the time-varying drift due to the wind field.

1. Quasi-Equilibrium-Glide Assumption

Consider an equilibrium gliding turn given by the condition $\dot{V} = \dot{\gamma} = \ddot{\psi} = 0$. Equations (1) and (2) imply

$$D = -W\sin\gamma \tag{11}$$

$$L\cos\sigma = W\cos\gamma \tag{12}$$

Dividing these two equations yields

$$\tan\gamma = -\frac{D}{L\cos\sigma} \tag{13}$$

In general, the equilibrium values of V and γ and the value of $\dot{\psi}$ are nonlinear functions of the state variables and canopy-specific performance parameters. For example, the nonlinear functional dependence may have the form

$$\gamma = \gamma(h, \sigma, L/D) \tag{14}$$

$$V = V(h, \sigma, W/S) \tag{15}$$

$$\dot{\psi} = \dot{\psi}(V, \sigma, L/D, \dot{\psi}_{\max}) \tag{16}$$

where the dependence of γ on h comes from the dependence of the apparent mass forces on air density. The form of Eqs. (14–16)

assumes that planning will be done at a constant value of ε. This is as far as we can go without making explicit assumptions about the aerodynamic and apparent mass forces. The following development will yield explicit forms for two of the preceding equations and simplify the form of the third.

It is convenient to specify the canopy performance in terms of the straight-line equilibrium values of the lift-to-drag ratio L/D and glide velocity V_0 at some specified altitude h_0 and the maximum turn rate $\dot{\psi}_{\max}$. Define the straight-line equilibrium-glide-path angle γ_G as

$$\tan\gamma_G = -\frac{D}{L} \tag{17}$$

Assuming that L/D remains constant with respect to σ (or implicitly with respect to the asymmetric flap deflection), from Eq. (13) we have

$$\tan\gamma = \frac{\tan\gamma_G}{\cos\sigma} \tag{18}$$

and from Eqs. (12) and (13) we have

$$\dot{\psi} = \frac{g}{V}\tan\sigma \tag{19}$$

A straight-line equilibrium glide will maintain constant dynamic pressure. This implies that the straight-line equilibrium-glide velocity V_G at an altitude h is given by

$$V_G = \left(\frac{\rho(h_0)}{\rho(h)}V_0^2\right)^{1/2} \tag{20}$$

Observe that V_0 includes the effects of wing loading, and V_G as defined in Eq. (20) includes the effects of altitude. This implies that the functional dependencies in Eq. (15) can be reduced to the nonturning velocity V_G and the bank angle σ: that is,

$$V = V(V_G, \sigma) \tag{21}$$

If one further assumes that the lift and drag coefficients remain constant with respect to σ, we can show that

$$V = \sqrt{\frac{V_G^2\cos\gamma}{\cos\gamma_G\cos\sigma}} \tag{22}$$

2. Change of Independent Variable

Without loss of generality we shall define the final time t_f as the time when $h = 0$. We see from Eqs. (6), (14), and (15) that t_f is dependent on the time history of σ. Define

$$\tau = h(t_0) - h(t) \tag{23}$$

We have $\tau = 0$ at $t = 0$ and $\tau = h(t_0)$ at $t = t_f$. In most practical scenarios τ is strictly increasing (as the altitude is strictly decreasing). Consider τ as the new independent variable. We have

$$\mathrm{d}\tau = -V\sin\gamma\,\mathrm{d}t \tag{24}$$

This change of variable offers several benefits. First, it lowers the order of the system by one, decreasing the computational cost of evaluating trajectories. Second, all trajectories from a given initial condition [with any arbitrary control history $u(\tau)$] have the same final time τ_f. Third, the wind profile is often known or easily expressed as a function of altitude. This property will be used in the next section to simplify the trajectory planning task by factoring out the influence of the wind. The key benefit of this variable change, though, is it converts the guidance task from a three-dimensional path planning problem to a two-dimensional problem.

To further simplify the trajectory planning problem, the turn acceleration dynamics are ignored. The new equations of motion incorporating this assumption and the quasi-equilibrium-glide assumption reduce to

$$\dot{x} = -\left(\frac{\cos\psi}{\tan\gamma} + \frac{w_x(\tau)}{V\sin\gamma}\right) \tag{25}$$

$$\dot{y} = -\left(\frac{\sin\psi}{\tan\gamma} + \frac{w_y(\tau)}{V\sin\gamma}\right) \tag{26}$$

$$\dot{\psi} = -\frac{g\tan\tilde{u}}{V^2\sin\gamma} \tag{27}$$

where $\tilde{u}$ is the commanded pseudo bank angle σ (control input).

3. Wind-Fixed Coordinate Frame

In the sequel we shall find it convenient to remove the τ-varying drift induced by the wind profile. Without loss of generality we shall fix the origin of the inertial coordinate frame at the targeted landing site with the x axis aligned with the desired final heading. Consider a second coordinate frame that moves with the air mass and has the same orientation as the inertial frame. The origin of this wind-fixed frame is located such that it exactly coincides with the origin of the inertial frame at $\tau = \tau_f$. The exact position in this coordinate frame is given by

$$x_w(\tau) = x(\tau) - \int_\tau^{\tau_f} \kappa(\tau)w_x(\tau)\,\mathrm{d}\tau \tag{28}$$

$$y_w(\tau) = y(\tau) - \int_\tau^{\tau_f} \kappa(\tau)w_y(\tau)\,\mathrm{d}\tau \tag{29}$$

where $\kappa = (V(\tau)\sin\gamma(\tau))^{-1}$. Thus, determining the exact position in this coordinate frame requires knowledge of the control history for the remaining portion of the trajectory (through the dependence of V and γ on $\dot{\psi}$). The position in this wind-fixed frame can be approximated by

$$x_w(\tau) = x(\tau) - \int_\tau^{\tau_f} \kappa_G(\tau)w_x(\tau)\,\mathrm{d}\tau \tag{30}$$

$$y_w(\tau) = y(\tau) - \int_\tau^{\tau_f} \kappa_G(\tau)w_y(\tau)\,\mathrm{d}\tau \tag{31}$$

where $\kappa_G = (V_G(\tau)\sin\gamma_G(\tau))^{-1}$. The velocity and flight-path angle magnitudes increase in a turn; thus, choosing the equilibrium-glide values of V and γ will tend to overestimate the total drift due to wind. However, this substitution provides a reasonable approximation to the position in the wind-fixed coordinate frame and significantly reduces computational cost.

Working in the wind-fixed frame further simplifies the motion planning problem, as the equations of motion (25–27) simplify to

$$\dot{x}_w = \tilde{a}\cos\psi \tag{32}$$

$$\dot{y}_w = \tilde{a}\sin\psi \tag{33}$$

$$\dot{\psi} = \tilde{a}u \tag{34}$$

where $\tilde{a} = -(\tan\gamma)^{-1}$, $u = 1/(r\cos\gamma)$, and the turning radius r is given by $(V^2\cos\gamma)/(g\tan\sigma)$. In the sequel we shall omit the subscript w unless the context is not clear.

C. Wind Field Modeling

In the most general case, the wind velocity vector has components along all three axes, which vary in space and time:

$$\mathbf{W} = \mathbf{W}(x, y, h, t) = \begin{bmatrix} w_x \\ w_y \\ w_z \end{bmatrix} \tag{35}$$

In the present work, we make the following assumptions about the wind profile:

1) The z axis component w_z is zero.

2) The horizontal wind can be written as the sum of a (relatively) low-frequency mean wind component and a (relatively) high-frequency turbulence component.

3) The mean wind components are functions of altitude and time only.

Oftentimes, if an a priori estimate of the wind profile is available, it will be given as a function of altitude. The mean wind profile can then be written as the sum of the altitude-varying a priori wind profile and a time-varying perturbation:

$$\mathbf{W} = \mathbf{W}_{ap}(h) + \tilde{\mathbf{W}}(t) \tag{36}$$

In light of the independent variable change defined in Eq. (23), we can write

$$\mathbf{W} = \begin{bmatrix} w_x \\ w_y \end{bmatrix} = \mathbf{W}_{ap}(\tau) + \tilde{\mathbf{W}}(\tau) \tag{37}$$

which justifies the τ dependence of w_x and w_y in Eqs. (32–34).

There are many potential sources for the a priori wind profile, such as radar observations, rapid-update-cycle forecast data [25], and balloon soundings or drop sondes [26]. In the event that no a priori wind profile is available or is believed to be inaccurate, $\mathbf{W}_{ap}$ can be set to zero and the entire mean wind field can be encompassed in the unknown wind field perturbation $\tilde{\mathbf{W}}(\tau)$.

III. Fixed-Time Trajectory Planning

In the previous section it was shown that the parafoil trajectory planning problem could be cast as a fixed-time two-point boundary-value problem. The planning problem consists of finding a kinematically feasible trajectory from an initial position and orientation $(x(0), y(0), \psi(0))$ to a final position and orientation $(x(\tau_f), y(\tau_f), \psi(\tau_f))$ [which, by the choice of coordinate frame discussed in the previous section, can be written (0,0,0)], where τ_f is the specified final time; that is, in the wind-fixed frame, the required terminal constraints are always

$$x(\tau_f) = 0 \tag{38}$$

$$y(\tau_f) = 0 \tag{39}$$

$$\psi(\tau_f) = 0 \tag{40}$$

This boundary-value problem is readily solved within the framework of optimal control, provided a meaningful performance index is defined. In this section we begin by deriving the conditions for a generalized trajectory optimization problem, which leads to insight into the nature of the optimal trajectories. We then proceed to derive minimum-time trajectories, which leads to a necessary condition for a kinematically feasible fixed-final-time trajectory to exist and the definition of a parameter, the altitude margin, that can be used in trajectory planning logic. Next, we present two methods for generating fixed-time trajectories, each particularly suited to certain classes of initial conditions and values of the altitude margin.

A. Optimal Control Problem

In this section we consider a generalized trajectory optimization problem. Much insight into the nature of the optimal control solutions can be obtained from the costate solutions to this problem. Recall that the optimal control problem is to find $u(t)$ to minimize the performance index

$$J = \int_0^{\tau_f} L(\mathbf{x}, u)\, \mathrm{d}\tau \tag{41}$$

subject to the constraints

$$\dot{\mathbf{x}} = \mathbf{f}(\mathbf{x}, u) \tag{42}$$

$$\mathbf{x}(\tau_0) \text{ given} \tag{43}$$

$$\Psi(\mathbf{x}(\tau_f)) = 0 \tag{44}$$

$$u \in U = [a, b] \tag{45}$$

where the dynamics in Eq. (42) are given by the kinematic model (32–34) with the velocity $\tilde{a}$ normalized to one, the state vector $\mathbf{x} = [\,x \quad y \quad \psi\,]^T$, and a and b are real scalars such that $a < 0 < b$. The terminal constraints (44) are defined in Eqs. (38–40). We assume that the function L in Eq. (41) is continuous in its arguments and not an explicit function of $\mathbf{x}$ or τ. The Hamiltonian for this system is given by

$$H = p_x \cos\psi + p_y \sin\psi + p_\psi u + L(\mathbf{x}, u) \tag{46}$$

where $\mathbf{p} = [\,p_x \quad p_y \quad p_\psi\,]^T$ is the adjoint or costate vector. The costate equations are

$$\dot{p}_x = -\frac{\partial H}{\partial x} = 0 \tag{47}$$

$$\dot{p}_y = -\frac{\partial H}{\partial y} = 0 \tag{48}$$

$$\dot{p}_\psi = -\frac{\partial H}{\partial \psi} = p_x \sin\psi - p_y \cos\psi \tag{49}$$

Substituting Eqs. (32) and (33) into Eq. (49), we get

$$\dot{p}_\psi = p_x \dot{y} - p_y \dot{x} \tag{50}$$

Observe from Eqs. (47) and (48) that p_x and p_y are constant. With this observation, integrating Eq. (49) with respect to τ yields

$$p_\psi = p_x y - p_y x - \tilde{c} \tag{51}$$

where $\tilde{c}$ is a constant of integration. We can also write

$$p_\psi = c_1 x + c_2 y + c_3 \tag{52}$$

where $c_1 = -p_y$, $c_2 = p_x$, and $c_3 = \tilde{c}$. Observe that $p_\psi = 0$ defines a line in the x–y plane and contours of constant p_ψ are lines parallel to this line. In the sequel we shall refer to the line $p_\psi = 0$ as the switching line for reasons that will become apparent.

Consider the variable change given by

$$p_x = b_1 \cos b_2 \qquad p_y = -b_1 \sin b_2 \tag{53}$$

for constants b_1 and b_2. Note that b_1 and b_2 can always be found such that this transformation holds for arbitrary p_x and p_y. The reverse transformation is given by

$$b_1 = (p_x^2 + p_y^2)^{1/2} \qquad b_2 = \tan^{-1}\left(-\frac{p_y}{p_x}\right) \tag{54}$$

Substituting Eq. (53) into Eq. (46), the Hamiltonian can now be written:

$$H = b_1 \cos(b_2 + \psi) + p_\psi u + L(\mathbf{x}, u) \tag{55}$$

Finally, we shall also find it convenient to rewrite the third costate equation using Eq. (53) as

$$\dot{p}_\psi = b_1 \sin(b_2 + \psi) \tag{56}$$

The minimum principle of Pontryagin states that along an optimal trajectory $(\mathbf{x}^*, \mathbf{p}^*)$, the optimal value of the control u^* minimizes the Hamiltonian over the set of all possible inputs at each moment in time: that is,

$$H(\mathbf{x}^*, \mathbf{p}^*, u^*, \tau) = \min_{u \in U, \tau \in [\tau_0, \tau_f]} H(\mathbf{x}^*, \mathbf{p}^*, u, \tau) \tag{57}$$

and that $\mathbf{p} \neq 0$ for $\tau \in [\tau_0, \tau_f]$.

B. Minimum-Time Trajectories

For minimum-time trajectories we have

$$L(\mathbf{x}, u) = 1 \tag{58}$$

The minimizing control u^* satisfying Eq. (57) is given by

$$p_\psi u^* \leq p_\psi u \quad \forall\ u \in U \tag{59}$$

If the minimizing control lies at one of the limits, then minimizing Eq. (55) implies

$$p_\psi u^* < 0 \tag{60}$$

If the minimizing control lies within the admissible region, we have

$$\frac{\partial H}{\partial u} = p_\psi = 0 \tag{61}$$

Because $p_\psi \equiv 0$, we must have $\dot{p}_\psi \equiv 0$, which, in light of Eq. (56), admits two possibilities. If $b_1 = 0$, then we have $p_x = p_y = p_\psi = 0$, which is ruled out by the minimum principle. If $b_1 \neq 0$, then either $\psi = -b_2$ or $\psi = -b_2 + \pi$ (both modulo 2π). Hence, $\dot{p}_\psi = 0 \Rightarrow \dot{\psi} = 0$ so that $u = 0$. Summarizing, we have

$$u = \begin{cases} a & p_\psi > 0 \\ 0 & p_\psi = 0 \\ b & p_\psi < 0 \end{cases} \tag{62}$$

The preceding discussion implies a number of properties for the minimum-time trajectories:

1) All optimal trajectories consist of maximum-rate turns and straight lines.

2) All straight-line segments are parallel to one fixed direction.

3) The line $p_\psi = 0$ divides the plane such that the control is strictly positive on one side and strictly negative on the other side.

4) All straight-line segments of the trajectory and all changes in turning direction occur on a single line in the plane.

The optimal minimum-time trajectory was shown by Dubins [10], and later by Boissonnat et al. [11], to consist of no more than three constant-control segments. Each segment is either a maximum-rate (minimum-radius) turn or a straight line ($u = 0$). Furthermore, the minimum-time trajectories are generated using one of six possible control sequences: RSR, RSL, LSR, LSL, LRL, or RLR where R corresponds to a maximum right-hand turn, L corresponds to a maximum left-hand turn, and S corresponds to a straight line. These trajectories are referred to as Dubins curves or Dubins paths. Examples of the RSL, LSL, and LRL Dubins paths are shown in Fig. 3. The circles in this figure correspond to the minimum turn radius.

C. Necessary Condition

Let the cost associated with each admissible Dubins path be denoted as τ_{RSR}, τ_{LSL}, etc., and define

$$\tau_{\min} = \min\{\tau_{\mathrm{RSR}}, \tau_{\mathrm{LSL}}, \tau_{\mathrm{RSL}}, \tau_{\mathrm{LSR}}, \tau_{\mathrm{RLR}}, \tau_{\mathrm{LRL}}\} \tag{63}$$

Clearly, for a trajectory satisfying the specified initial conditions and terminal conditions and for the specified final time τ_f to exist, we require that

$$\tau_{\min} \leq \tau_f \tag{64}$$

Now let τ_{360} equal the cost of completing one full 360 deg turn at maximum turn rate. We now define the altitude margin as

$$\eta = \frac{\tau_f - \tau_{\min}}{\tau_{360}} \tag{65}$$

so that the necessary condition (64) can also be written as

$$\eta \geq 0 \tag{66}$$

Considering the definition of τ in Eq. (23), one can see that the altitude margin is a normalized measure of the altitude in excess of the minimum altitude required for the constrained system to reach the specified terminal conditions from the specified initial conditions. The altitude margin provides a quantitative measure of the difficulty in attaining the final conditions in the specified time interval. An altitude margin of zero indicates that the initial altitude is exactly the required altitude to reach the final condition. A negative value of the altitude margin indicates that the initial altitude is not sufficient to reach the final conditions for any choice of the control history $u(\tau)$. A positive altitude margin indicates that the amount of excess energy (altitude) is available for maneuvering and the degree of wind uncertainty that can be overcome.

D. Minimum-Control-Energy Paths

Consider now the case in which the final time is *fixed* at τ_f and the performance index is the control energy [18]:

$$L(\mathbf{x}, u) = \tfrac{1}{2}u^2 \tag{67}$$

The minimizing control u^* satisfying Eq. (55) is given by

$$p_\psi u^* + \tfrac{1}{2}u^{*2} \leq p_\psi u + \tfrac{1}{2}u^2 \quad \forall\ u \in U \tag{68}$$

As before, if the minimizing control lies at one of the limits, then minimizing Eq. (55) implies

$$p_\psi u < 0 \tag{69}$$

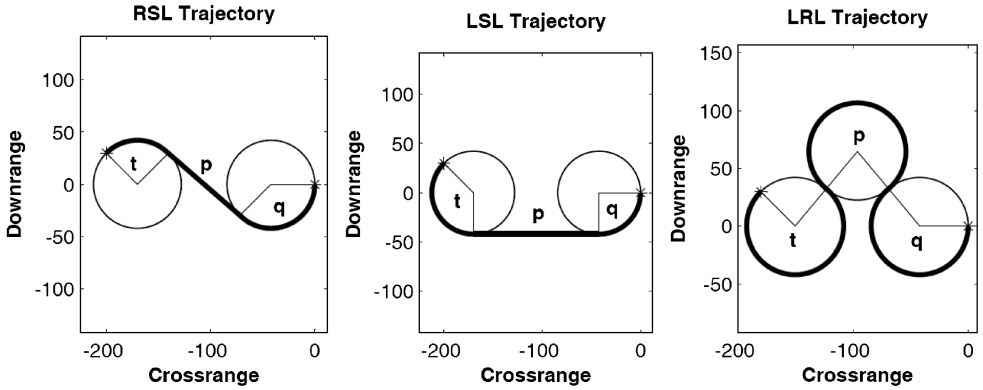

Fig. 3 Examples of Dubins paths: RSL (left), LSL (center), and LRL (right). Note that the LRL path is not optimal in this example. The quantities *t* and *q* are the outer turn angles and the quantity *p* is the length of the straight-line segment for type RSR, RSL, LSR, and LSL paths and the middle turn angle for type LRL and RLR paths.

If the minimizing control lies in the interior of the admissible control set, we have

$$\frac{\partial H}{\partial u} = p_\psi + u = 0 \tag{70}$$

Summarizing, we have

$$u = \begin{cases} a & -p_\psi < a \\ -p_\psi & -p_\psi \in [a, b] \\ b & -p_\psi > b \end{cases} \tag{71}$$

Using Eqs. (52) and (70), the guidance law in the absence of control saturation can be written

$$u = -(c_1 x + c_2 y + c_3) \tag{72}$$

We now illustrate some properties of the optimal trajectories. Observe from Eq. (72) that $u = 0$ defines the parametric line

$$c_1 x + c_2 y + c_3 = 0 \tag{73}$$

which is the same as the switching line defined in Eq. (52).

Property 1. The control u can be written as

$$u = d\sqrt{c_1^2 + c_2^2} \tag{74}$$

where d is the signed perpendicular distance of the point (x, y) from the line given by Eq. (73).

Proof. The signed perpendicular distance d of a point (x, y) from the general parametric line $ax + by + c = 0$ can be shown to be $(ax + by + c)/\sqrt{a^2 + b^2}$. Substituting $a = c_1$, $b = c_2$, and $c = c_3$ completes the proof.

Property 2. Line (73) divides the x–y plane so that the control u is strictly positive on one side of the line and strictly negative on the other. The proof follows directly from Property 1, observing that c_1 and c_2 are constant.

Property 3. In general, the trajectory resulting from the guidance law (72) contains no straight line.

Proof. A straight-line trajectory requires $u \equiv 0$. Observe that u remains zero only when the trajectory lies along the line (73). If any portion of the trajectory lies along this line the entire trajectory must lie along the line as $u = 0 \Rightarrow \dot{\psi} = 0$. Only the trivial case in which the entire trajectory lies on the negative x axis contains a straight line. This is a pathological case in which the initial condition lies exactly on the negative x axis with an initial heading of zero and the specified final time is such that the system just reaches the target.

Property 4. In the absence of turn rate limit, the trajectories contain no circular arcs.

Proof. Suppose the trajectory contains a circular arc. This means that u is a nonzero constant and $\dot{u} = 0$ and for some finite time interval. By Eq. (72), $\dot{u} = 0$ for the unsaturated u implies that

$$c_1 \dot{x} = -c_2 \dot{y} \tag{75}$$

which, by Eqs. (32) and (33), in turn, results in that

$$-\frac{c_1}{c_2} = \tan\psi = \text{constant} \tag{76}$$

However, the preceding condition of constant ψ contradicts the requirement of nonzero constant $u = \dot{\psi}$. Thus, the trajectories cannot contain circular arcs in the absence of turn rate limit.

As discussed in Sec. III.B, the Dubins paths consist of a series of circular arcs and straight-line segments. The preceding properties 3 and 4 indicate that the minimum-control-energy trajectories in general will not coincide with Dubins paths.

E. Solution and Sample Minimum-Control-Energy Trajectories

The solution to the preceding fixed-time minimum-control-energy problem is ensured whenever the problem admits feasible solutions. More specifically, if any feasible trajectory exists that satisfies the given initial condition and terminal constraints at τ_f with an admissible control $u(\tau) \in U$ for $0 \le \tau \le \tau_f$, this optimal control problem is guaranteed to have a solution. This conclusion directly follows corollary 2 of chapter 4 in [27], because the system equations in Eq. (42) are affine in the control u, and for any fixed $\mathbf{x}$ the set $\{L(\mathbf{x}, u)\mathbf{f}(\mathbf{x}, u)\}, \forall\ u \in U$, is strictly convex in R^4 (where $U = [a, b]$ is compact and convex). This property is very reassuring for our purpose of trajectory planning.

To determine the solution, the required values of c_1, c_2, and c_3 in Eq. (72) need to be found numerically to satisfy the terminal condition in Eqs. (38–40). The problem can be cast as a nonlinear root-finding problem. The convergence behavior is dependent on both the initial offset of the system from the target and the altitude margin. For sufficient altitude margin, the solution is found easily with a wide range of initial guesses. For large offsets, small changes in c_1, c_2, and c_3 lead to large changes in the final position. Hence, convergence tends to be become more sensitive with respect to initial guesses as the initial offset becomes very large (greater than 10^3 in consistent units). As the altitude margin decreases, the convergence behavior also becomes increasingly dependent on the initial guess of the solution. In general, if the normalized altitude margin is less than about one, it becomes considerably more difficult to converge. This is because, in such cases, the trajectory gets close to the minimizing Dubins path, but the minimum-control-energy trajectories cannot converge directly to the Dubins path (cf. properties 3 and 4 in the preceding section).

A number of example trajectories are shown in Fig. 4. Each trajectory has the same starting position and the initial altitude is such that the initial normalized altitude margin is three. But the initial heading is different. The figure shows the general shape of the trajectories computed using the presented optimal control approach (recall that the targeted landing site is at the origin).

A number of example trajectories with the same starting configuration are shown in Fig. 5. For these trajectories, the altitude margin is varied from 0.2 to 2.2 in increments of 0.4. A feature worth noting in Fig. 5 is that as the altitude margin decreases, the trajectory begins to approach to the Dubins path, indicated by the dotted line.

Another example trajectory is shown in Fig. 6. This is a pathological example in which the initial position is directly above the desired target with the initial heading opposite the desired final heading. The initial normalized altitude margin is relatively large at 10. Observe the symmetry of the trajectory about the downrange axis, which is due to the initial condition. For this case, the value of c_2 in the guidance law is zero. This example illustrates that the trajectory generation method is robust to cases with obscure initial conditions and a large initial altitude margin.

F. Modified Dubins Paths

The minimum-time Dubins paths in Sec. III.B cannot be directly applied to our problem because it is a *fixed-time* problem. However, it is possible to modify the Dubins path calculation to generate fixed-time reference trajectories for cases in which the altitude margin is greater than or equal to zero. In this case the trajectory is no longer optimal in any sense, but we will show that a simple closed-form expression can be used to generate the modified Dubins path. The idea is to increase the turn radius from the minimum until the altitude margin (using the new turn radius) of the resulting path is equal to zero; in other words, the cost of the path is increased until the cost equals the specified terminal time. A path generated in this fashion satisfies the initial and final conditions imposed on the trajectory, as well as the fixed final time (altitude margin).

The turning radius is defined by

$$r = \frac{V^2 \cos\gamma}{g \tan\sigma} \tag{77}$$

where γ given by Eq. (14) or Eq. (18) and V given by Eq. (15) or Eq. (22) are functions of σ. Given an initial position and orientation (x_0, y_0, ψ_0), a final position and orientation (x_f, y_f, ψ_f), and turning radius r (or, implicitly, σ), one can find an analytical expression for

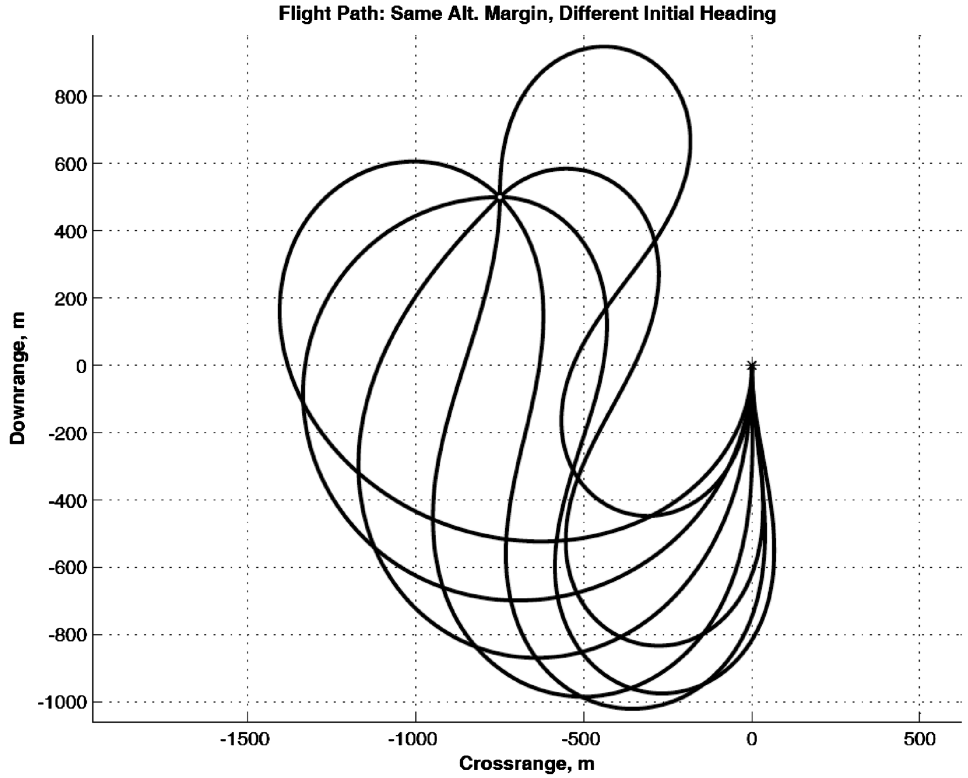

Fig. 4 Minimum-control-energy trajectories for an initial normalized altitude margin $\eta = 3$, varying the initial heading. The initial position is the same for each case.

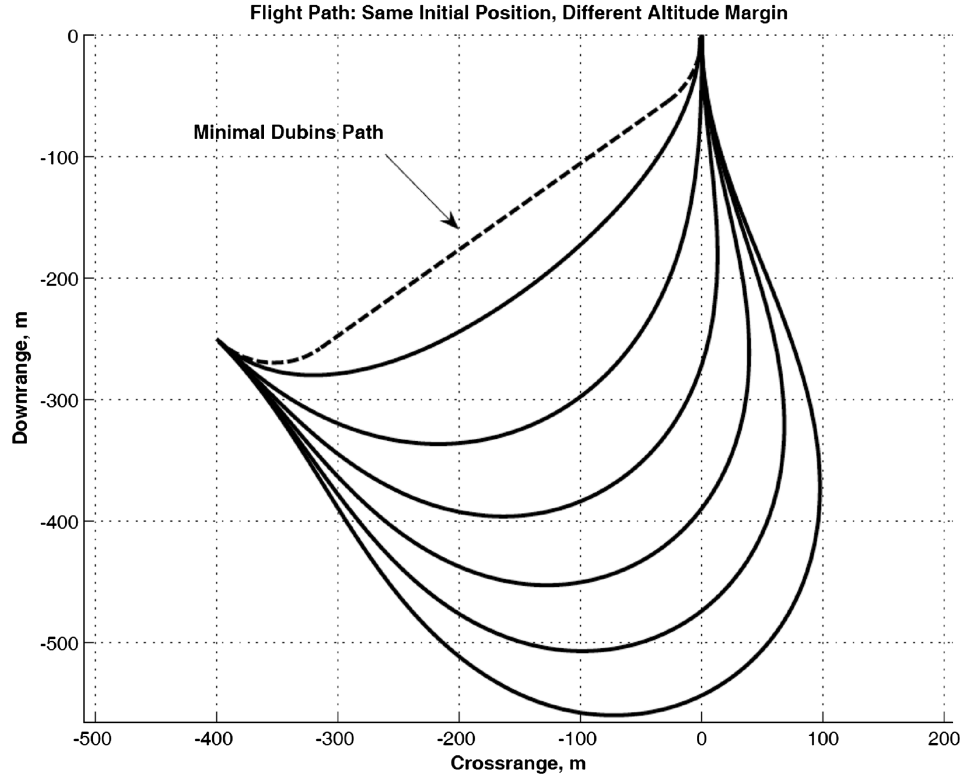

Fig. 5 Minimum-control-energy trajectories for the same initial configuration, varying the initial normalized altitude margin η from 0.2 to 2.2 in increments of 0.4. The dotted line corresponds to the minimal Dubins path.

the quantities t, p, and q defined in Fig. 3 as well as the cost for each of the admissible Dubins paths. Figure 7 illustrates the geometry of the problem and defines some key parameters that will be used in the following development.

From Fig. 7 we see that

$$\Gamma = \tan^{-1}\left(\frac{y_f - y_0}{x_f - x_0}\right) \tag{78}$$

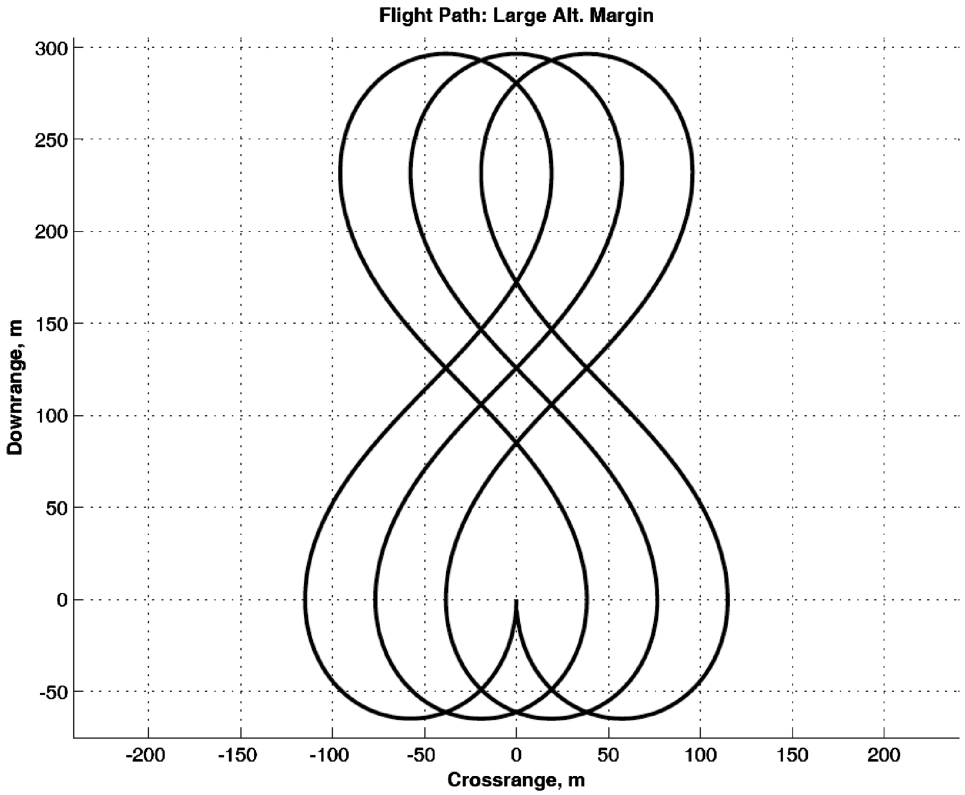

Fig. 6 This is an example trajectory with the initial position at the intended target and the initial heading opposite the required final heading. The normalized altitude margin for this example is 10. Note the symmetry of the trajectory about the downrange axis.

$$\lambda = \Gamma - \psi_0 \{\text{mod} 2\pi\} \tag{79}$$

$$\mu = \Gamma - \psi_f \{\text{mod} 2\pi\} \tag{80}$$

$$d = ((x_f - x_0)^2 + (y_f - y_0)^2)^{1/2} \tag{81}$$

Recall that Dubins path consists of three segments of elementary motion: turning right along an arc with radius r (denoted by R), turning left along an arc of the same radius r (L), and motion in a straight line (S). We will limit the sequence of motion primitives to the six sequences corresponding to the minimum-time Dubins paths described in Sec. III.B: RSR, RSL, LSR, LSL, LRL, or RLR. Suppose the system is at the point (x_1, y_1, ψ_1) and then performs a right turn through an angle ν. Following the approach in [28], define an operator R_ν that transforms the point (x_1, y_1, ψ_1) to the point at the end of the turn, denoted as (x_2, y_2, ψ_2). Similar operators L_ν and S_ν can be defined for left turns and straight-line segments, respectively. These operators are given by

$$R_\nu(x_1, y_1, \psi_1) = \begin{pmatrix} x_1 + r\sin(\psi_1 + \nu) - r\sin\psi_1 \\ y_1 - r\cos(\psi_1 + \nu) + r\cos\psi_1 \\ \psi_1 + \nu \end{pmatrix} \tag{82}$$

$$L_\nu(x_1, y_1, \psi_1) = \begin{pmatrix} x_1 - r\sin(\psi_1 - \nu) + r\sin\psi_1 \\ y_1 + r\cos(\psi_1 - \nu) - r\cos\psi_1 \\ \psi_1 - \nu \end{pmatrix} \tag{83}$$

$$S_\nu(x_1, y_1, \psi_1) = \begin{pmatrix} x_1 + \nu\cos\psi_1 \\ y_1 + \nu\sin\psi_1 \\ \psi_1 \end{pmatrix} \tag{84}$$

Consider a new coordinate frame found by rotating the coordinate frame in Fig. 7 clockwise by an angle Γ with the origin located at the initial point (x_0, y_0). In this new frame, the initial position and orientation are $(0, 0, \lambda)$ and the final position and orientation are $(d, 0, \mu)$. By composition of the operators (82–84), one can find analytical expressions for the turn angles or line lengths t, p, and q defined in Fig. 3. For example, the result of an RSL turn can be found by the composition $L_q(S_p(R_t(0, 0, \lambda)))$. Using the final condition $(d, 0, \mu)$ leads to the scalar system of equations

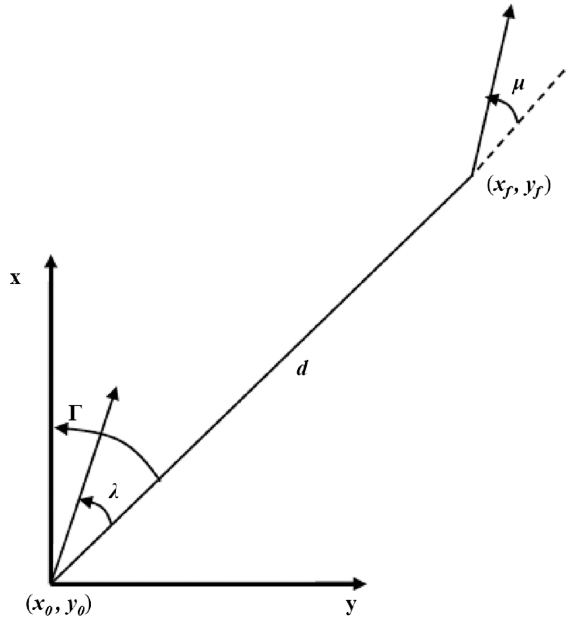

Fig. 7 Geometry and parameters used to calculate members of the Dubins set.

$$
\begin{aligned}
d &= p\cos(\lambda + t) + 2r\sin(\lambda + t) - r\sin\lambda - r\sin\mu \\
0 &= p\sin(\lambda + t) - 2r\cos(\lambda + t) + r\cos\lambda + r\cos\mu \\
\mu &= \lambda + t - q
\end{aligned} \tag{85}
$$

which can be solved to yield the corresponding lengths of the trajectory segments:

$$
\begin{aligned}
t_{\mathrm{RSL}} &= -\lambda - \tan^{-1}\left(\frac{2r}{p}\right) + \tan^{-1}\left(\frac{-r\cos\lambda - r\cos\mu}{d + r\sin\lambda + r\sin\mu}\right) \\
q_{\mathrm{RSL}} &= -\mu - \tan^{-1}\left(\frac{2r}{p}\right) + \tan^{-1}\left(\frac{-r\cos\lambda - r\cos\mu}{d + r\sin\lambda + r\sin\mu}\right) \\
p_{\mathrm{RSL}} &= (-2r^2 + d^2 + 2r^2\cos(\lambda - \mu) + 2rd(\sin\mu + \sin\lambda))^{1/2}
\end{aligned} \tag{86}
$$

The cost (which is time, or the altitude drop for the parafoil) of the RSL path can be shown to be

$$
\tau_{\mathrm{RSL}} = r\tan\gamma(\lambda - \mu + 2t_{\mathrm{RSL}}) + p_{\mathrm{RSL}}\tan\gamma_G \tag{87}
$$

In a similar fashion we can find t, p, and q and the cost for the remaining Dubins paths. For LSR we have

$$
\begin{aligned}
t_{\mathrm{LSR}} &= \lambda + \tan^{-1}\left(\frac{2p}{r}\right) - \tan^{-1}\left(\frac{r\cos\lambda + r\cos\mu}{d - r\sin\lambda - r\sin\mu}\right) \\
q_{\mathrm{LSR}} &= \mu + \tan^{-1}\left(\frac{2p}{r}\right) - \tan^{-1}\left(\frac{r\cos\lambda + r\cos\mu}{d - r\sin\lambda - r\sin\mu}\right) \\
p_{\mathrm{LSR}} &= (-2r^2 + d^2 + 2r^2\cos(\lambda - \mu) - 2rd(\sin\mu + \sin\lambda))^{1/2}
\end{aligned} \tag{88}
$$

$$
\tau_{\mathrm{LSR}} = r\tan\gamma(\mu - \lambda + 2t) + p\tan\gamma_G \tag{89}
$$

For RSR we have

$$
\begin{aligned}
t_{\mathrm{RSR}} &= -\lambda - \tan^{-1}\left(\frac{r\cos\mu - r\cos\lambda}{d + r\sin\lambda - r\sin\mu}\right) \\
q_{\mathrm{RSR}} &= \mu\{\mathrm{mod}2\pi\} - \tan^{-1}\left(\frac{r\cos\mu - r\cos\lambda}{d + r\sin\lambda - r\sin\mu}\right) \\
p_{\mathrm{RSR}} &= (2r^2 + d^2 - 2r^2\cos(\lambda - \mu) + 2rd(\sin\mu - \sin\lambda))^{1/2}
\end{aligned} \tag{90}
$$

$$
\tau_{\mathrm{RSR}} = r\tan\gamma(\mu - \lambda + 2t) + p\tan\gamma_G \tag{91}
$$

For LSL we have

$$
\begin{aligned}
t_{\mathrm{LSL}} &= \lambda - \tan^{-1}\left(\frac{r\cos\lambda - r\cos\mu}{d - r\sin\lambda + r\sin\mu}\right) \\
q_{\mathrm{LSL}} &= -\mu\{\mathrm{mod}2\pi\} + \tan^{-1}\left(\frac{r\cos\lambda - r\cos\mu}{d - r\sin\lambda + r\sin\mu}\right)\{\mathrm{mod}2\pi\} \\
p_{\mathrm{LSL}} &= (2r^2 + d^2 - 2r^2\cos(\lambda - \mu) + 2rd(\sin\mu - \sin\lambda))^{1/2}
\end{aligned} \tag{92}
$$

$$
\tau_{\mathrm{LSL}} = r\tan\gamma(\lambda - \mu) + p\tan\gamma_G \tag{93}
$$

For LRL we have

$$
\begin{aligned}
t_{\mathrm{LRL}} &= \lambda + \frac{p}{2} - \tan^{-1}\left(\frac{r\cos\lambda - r\cos\mu}{d - r\sin\lambda + r\sin\mu}\right) \\
q_{\mathrm{LRL}} &= \lambda - t_{\mathrm{LRL}} + p_{\mathrm{LRL}} - \mu \\
p_{\mathrm{LRL}} &= \cos^{-1}\left[\frac{1}{8}\left(6 + 2\cos(\lambda - \mu) + \frac{2d}{r}(\sin\lambda - \sin\mu) - \frac{d^2}{r^2}\right)\right]
\end{aligned} \tag{94}
$$

$$
\tau_{\mathrm{LRL}} = r\tan\gamma(\lambda - \mu + 2p) \tag{95}
$$

And, finally, for RLR we have

$$
\begin{aligned}
t_{\mathrm{RLR}} &= \left(-\lambda + \frac{p}{2} + \tan^{-1}\left(-\frac{r\cos\lambda + r\cos\mu}{d + r\sin\lambda - r\sin\mu}\right)\right) \\
q_{\mathrm{RLR}} &= \mu - \lambda - t_{\mathrm{LRL}} + p_{\mathrm{LRL}} - \mu \\
p_{\mathrm{RLR}} &= \cos^{-1}\left[\frac{1}{8}\left(6 + 2\cos(\lambda - \mu) - \frac{2d}{r}(\sin\lambda - \sin\mu) - \frac{d^2}{r^2}\right)\right]
\end{aligned} \tag{96}
$$

$$
\tau_{\mathrm{RLR}} = r\tan\gamma(\mu - \lambda + 2p) \tag{97}
$$

To find a modified Dubins path with a fixed final time we select an initial guess value for σ, from which γ, V, and r are calculated by Eqs. (18), (22), and (77), respectively. The cost (time) of the Dubins path is then computed. The value of σ is iterated on using a secant method until the time of the modified Dubins path equals the specified final time for the trajectory. This process is done in a preferred order among the six possible turn sequences, starting with the sequence corresponding to the minimum-time path and then in the order of RSR, LSL, RSL, LSR, LRL, and RLR. When the solution is found for a path, the process stops and no further search is done. Only when it is determined that the solution does not exist for a particular turn sequence is the search continued using the next sequence.

The convergence of this method is well-behaved as long as the distance between the turn centers is sufficiently large and/or the normalized altitude margin is less than one. One can see from the preceding equations that the cost of each Dubins path (i.e., τ_{RSR}, τ_{LSL}, τ_{RSL}, τ_{LSR}, τ_{RLR}, and τ_{LRL}) is at least piecewise-continuous in r. However, not all Dubins paths exist for a given set of initial conditions (λ, μ, and d) and a given r. For example, we see that the RSL and LSR paths fail to exist when r is increased beyond a certain threshold (as p_{RSL} and p_{LSR} become imaginary). Similarly, the LRL and RLR paths fail to exist when r is decreased beyond a certain threshold (as p_{RLR} and p_{LRL} become imaginary). The RSR and LSL paths exist for all $r > 0$; however. τ_{RSR} and τ_{LSL} are piecewise-continuous in r, where a jump discontinuity exists for sufficiently large r. What all this means is that there are cases for which no modified Dubins path exists with a cost equal to the specified τ_f, even though a feasible trajectory does exist in the case that leads from the given initial condition to the specified final condition at the specified final time. This possibility of nonexistence of modified Dubins path in a feasible case arises as a consequence of limiting the search for trajectory in a finite-dimensional space defined by the six path sequences, whereas the original problem is in infinite-dimensional functional space. Expanding the number of path sequences may remedy some of the cases but cannot eliminate the problem, as the expanded search space is still finite-dimensional. In [12] an extended set of turn sequence is used for trajectory search using Dubins paths. Still, the nonexistence problem is noted in certain cases.

IV. Onboard Trajectory Planning and Guidance

Given the initial condition of the parafoil, the trajectory planning algorithms in Sec. III are called onboard to generate a reference trajectory that satisfies all the required conditions/constraints. This reference trajectory provides the guidance information for the parafoil. If the trajectory planning algorithms are called in every guidance cycle to generate the trajectory based on the current navigation data, the profiles from the resulting trajectory provides closed-loop guidance. The guidance is closed-loop in the sense that the guidance commands depend on the current condition. Our proposed trajectory planning/guidance strategy is a hybrid combination of modified Dubins paths and the minimum-control-energy paths. The reason for the hybrid approach is to take the advantage of the strengths of minimum-control-energy and modified-Dubins-path techniques have to offer so as to ensure the solution of a planned trajectory in all feasible cases. The minimum-control-energy paths

are desired to ease the power requirements of the system by reducing control-line winch activity, and the solution is guaranteed to exist as long as the altitude margin is adequate. But robustness of convergence of the search process for the solution requires that the position offset from the target is not excessively large and the normalized altitude margin is greater than approximately one. On the other hand, the modified Dubins path converges well for large offset distances and altitude margins below one, but may suffer from nonexistence of the solution for the particular set of initial conditions and given time (altitude margin) in certain other cases.

Recall that the altitude margin η is the excess maneuvering altitude normalized by the altitude required to complete one full turn at maximum turn rate. At each guidance cycle the reference trajectory from the current position, orientation (azimuth), and altitude to the final position, orientation, and altitude is computed from the following steps:

1) Determine the initial position in the wind-fixed coordinate frame.

2) Determine the altitude required to complete all admissible Dubins paths.

3) Determine the normalized altitude margin η from the optimal (minimum-time) Dubins path.

4) Determine the type of reference trajectory to calculate based on the following:

a) If $\eta > 5$ compute an energy management trajectory (discussed subsequently).

b) If $1 < \eta \leq 5$ compute a minimum-control-energy trajectory.

c) If $0 \leq \eta \leq 1$ compute a modified Dubins trajectory.

d) If $\eta < 0$ track directly toward the target to minimize the miss distance.

5) Calculate and store $x_d(\tau)$, $y_d(\tau)$, and $\theta_d(\tau)$.

If at any guidance cycle the specified trajectory generation method fails to converge, an attempt is made using the other trajectory generation method. If neither method converges at a given guidance cycle for any reason, the last known trajectory is used for the reference trajectory. The reference trajectory can be replanned at a specified update rate or, alternatively, the replanning can be performed only when the trajectory tracking error exceeds a specified threshold.

The energy management trajectory mentioned previously is a Dubins path from the current position to a nominal radius circle centered three minimum-turn diameters from the origin in the wind-fixed frame. The nominal radius is specified by a turn rate equal to 80% of the specified maximum turn rate of the system. The center lies along lines passing through the origin at ± 45 deg. The circle is located in the quadrant containing the current position of the system. The circle is tracked until the first guidance cycle update in which $\eta \leq 5$. The idea behind this strategy is to bring the system close to the target using as little maneuvering energy as possible. This minimizes the potential drift due to uncertainty in the wind and canopy over- or underperformance. The position of the final turn circle is chosen to allow plenty of maneuvering room when the system exits the energy management phase and to promote rapid convergence of the terminal-phase reference trajectory.

An example high-margin trajectory is shown in Fig. 8. In this case the system has an L/D of 1, an airspeed of 12 m/s, and a maximum turn rate of 15 deg /s. There is no wind in this case to highlight the shape and form of the trajectory. The initial altitude margin for this case was approximately 7.

Observe that the guidance logic is parameterized completely in terms of η, which is derived from the specified parafoil performance parameters (L/D, V_0, and $\dot{\psi}_{\max}$) and the current conditions. Furthermore, the reduced-order model used to generate the reference trajectories also uses these parameters. In this way, the guidance algorithm is fully adaptable to parafoil canopies with a wide range of performance characteristics. More specifically, the guidance algorithm has the potential to require little or no tuning to accommodate variations in canopy performance.

Another key difference between this algorithm and some previous parafoil guidance algorithms (e.g., [1,6]) is that the reduction of excess energy is performed near the end of the trajectory rather than early in the trajectory. This tends to make the algorithm more robust

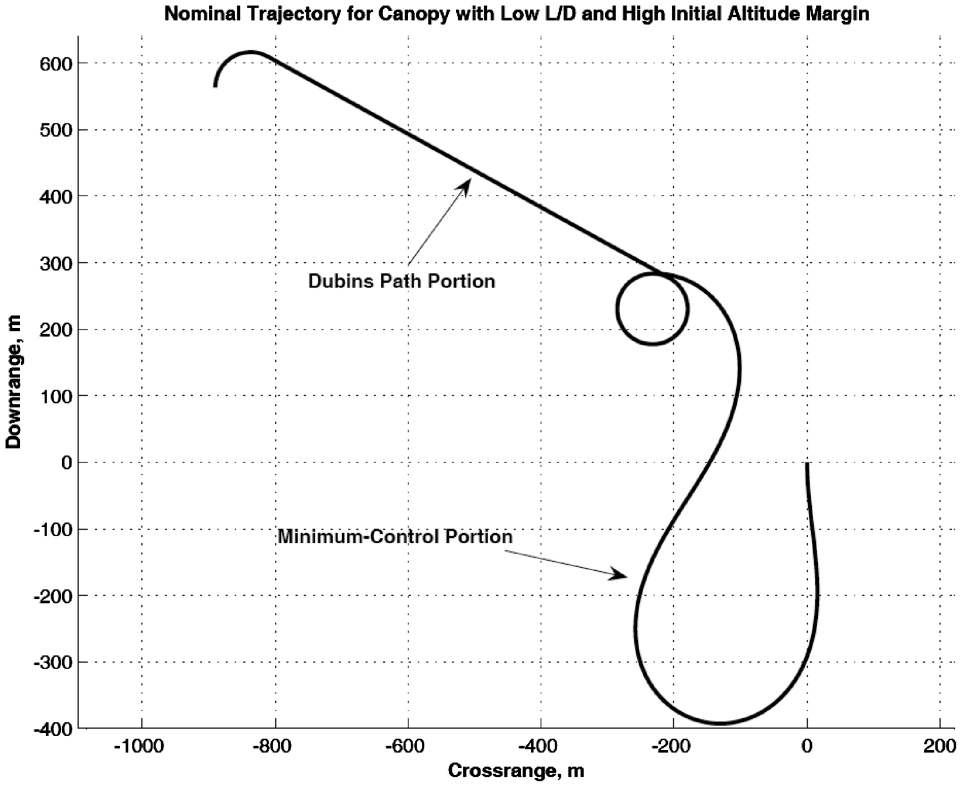

Fig. 8 An example of a case with a high initial altitude margin ($\eta \cong 7$) for a canopy with $L/D = 1$, $V_0 = 12$ m/s, and $\dot{\theta}_{\max} = 15$ deg /s. The initial Dubins path portion of the energy management phase is clearly distinguished in the upper-left portion of the figure. The terminal phase of the trajectory can be seen in the lower-right portion of the figure.

to unknown variations in the wind profile as well as errors in the model used for trajectory planning.

V. Trajectory Tracking Control

Once the trajectory has been planned, the parafoil is controlled to fly the planned trajectory until the reference trajectory is replanned/updated. In this section we present a baseline control design for trajectory tracking. Let the reference trajectory be given by

$$\mathbf{x}^* = \begin{bmatrix} x^*(\tau) \\ y^*(\tau) \\ \psi^*(\tau) \end{bmatrix} \tag{98}$$

and define the tracking error components to be

$$e_1 = x(\tau) - x^*(\tau) \qquad e_2 = y(\tau) - y^*(\tau) \qquad e_3 = \psi(\tau) - \psi^*(\tau) \tag{99}$$

By rotating the tracking error components e_1 and e_2 through an angle ψ^* we can define the along-track and cross-track errors as

$$e_{\text{atrack}} = e_1 \cos\psi^* + e_2 \sin\psi^* \qquad e_{\text{xtrack}} = e_1 \sin\psi^* - e_2 \cos\psi^* \tag{100}$$

The time rate of change of the cross-track error using t rather than τ as the independent variable can be shown to be

$$\begin{aligned} \dot{e}_{\text{xtrack}} &= (\dot{x} - \dot{x}^*)\sin\psi^* - (\dot{y} - \dot{y}^*)\cos\psi^* \\ &\quad + ((x - x^*)\cos\psi^* + (y - y^*)\sin\psi^*)\dot{\psi}^* \end{aligned} \tag{101}$$

where $\dot{\psi}^*$ is known given the reference trajectory. From Eqs. (4) and (5) we see that to accurately determine $\dot{x}$ and $\dot{y}$ in the wind-fixed coordinate frame requires measurement of the vehicle airspeed and flight-path angle. Accurate measurement of both of these quantities is often difficult and increases the size and weight of the GNC hardware. As such, we use values provided from the equilibrium-glide assumption to approximate the cross-track error derivative as

$$\begin{aligned} \dot{e}_{\text{xtrack}} &= V_T \cos\gamma_T[(\cos\psi - \cos\psi^*)\sin\psi^* \\ &\quad - (\sin\psi - \sin\psi^*)\cos\psi^*] \\ &\quad + ((x - x^*)\cos\psi^* + (y - y^*)\sin\psi^*)\dot{\psi}^* \\ &= -V_T \cos\gamma_T \sin e_3 + (e_1 \cos\psi^* + e_2 \sin\psi^*)\dot{\psi}^* \end{aligned} \tag{102}$$

A linearized analysis of the parafoil model in Eqs. (1–8) shows that the cross-track error dynamics cannot be stabilized by using only proportional feedback control. Therefore, we propose a proportional-plus-derivative control law for the cross-track control channel so that the commanded input is given by

$$\sigma_{\text{com}} = \sigma^* + k_{p_{\text{lat}}} e_{\text{xtrack}} + k_d \dot{e}_{\text{xtrack}} \tag{103}$$

where σ^* is the modeled bank angle corresponding to $\dot{\psi}^*$, and $k_{p_{\text{lat}}} > 0$ and $k_d > 0$ are appropriately selected constants.

An analysis on the linearized dynamics in Eqs. (1–8) indicates the along-track error can be stabilized by using just proportional feedback control. For parafoil systems for which longitudinal control is available, we propose a proportional control law for the along-track control channel so that the commanded input is given by

$$\varepsilon_{\text{com}} = k_{p_{\text{lon}}} e_{\text{atrack}} \tag{104}$$

where we note $\varepsilon_{\text{trim}} = 0$ as discussed previously, and $k_{p_{\text{lon}}} > 0$ is an appropriately selected constant.

VI. Simulation Results

A series of Monte Carlo simulations are performed to study the effects of sensor errors and uncertainty in the a priori wind profile, payload mass, and canopy performance. To evaluate the GNC concept, the model in Eqs. (1–8) is used to represent the true motion of the parafoil. The aerodynamic model from [22] using parameters given in Table 1 is used to generate the lift and drag coefficients as functions of the symmetric flap (brake) deflection and rigging angle. Here, we assume that $\dot{\alpha} = 0$ and use the value of α corresponding to a pitching moment of zero. Data are given for rigging angles ranging from −4 to 10 deg at symmetric flap settings of zero, half, and full deflection. We choose to use symmetric flap setting for longitudinal control and select a rigging angle of 4 deg and a trim flap setting of 70% brakes, which gives L/D equal to 2.1. The allowable range of symmetric flap deflection is from 50 to 90%, which allows L/D to vary from 1.7 to 2.9.

Using the preceding aerodynamic model, we consider two parafoils with significant differences in performance. Parafoil 1 represents a typical small- to midscale system characterized by a moderate maximum turn rate and moderate to fast control response. We consider a maximum turn rate of 30 deg/s and a canopy area of 25 m^2 that is lightly loaded at 5 kg/m^2, which leads to a glide airspeed of 9.27 m/s and a minimum turn radius of 15.7 m. Parafoil 2 represents a typical large-scale system that is characterized by a slow maximum turn rate and slow control response. We consider a maximum turn rate of 10 deg/s and a canopy area of 560 m^2 that is highly loaded at 20 kg/m^2, which leads to a glide airspeed of 18.5 m/s and a minimum turn radius of 98.1 m. These and other parameters required for the simulation and guidance algorithm are summarized in Table 2. The trajectory planning algorithm uses a maximum turn rate that is 80% of the nominal value both to increase robustness to parameter uncertainty and to allow sufficient control margin for the tracking controller. The trajectory is replanned whenever the tracking error exceeds 10 m, but at a maximum update rate of 0.2 Hz. The maximum update rate prevents chatter in switching between trajectory types due to lag in the control system. After an initial trajectory has been computed, subsequent trajectory calculations typically converge rapidly, often requiring only a few iterations.

Real-world wind data are used in all simulations. The wind profiles are randomly selected from a database containing the daily National Oceanic and Atmospheric Administration balloon sounding profiles [29]. The wind data are linearly interpolated between data points and the wind speeds are scaled so that they do not exceed 30 m/s. Phenomena such as shear layers and vertical drafts are not considered in the present study. Note that a primary assumption in Sec. II.B is that τ is strictly increasing (i.e., altitude is strictly decreasing). On relatively uncommon occasions, a parafoil may enter pockets with updrafts strong enough to increase the altitude. In such cases, the effect of the altitude increase is to increase the tracking error. The trajectory tracking controller will attempt to correct the tracking

Table 1 Parameters used to generate C_L and C_D vs symmetric brake deflection using [22]

Canopy area S	28 m^2
Aspect ratio A	2.0
Canopy mass m_c	5 kg
Payload mass m_p	135 kg
Ratio of line length to canopy span R/b	1.0
Number of lines n	40
Line diameter d	0.0035 m

Table 2 Parameters required by the guidance algorithm and for the simulation

Parameter	Parafoil 1	Parafoil 2
Equilibrium glide velocity V_0	9.27 m/s	18.5 m/s
Equilibrium glide-path angle γ_G	−25.2 deg	−25.2 deg
Maximum turn rate $\dot{\psi}_{\max}$	30 deg/s	10 deg/s
Maximum bank rate $\dot{\sigma}_{\max}$	30 deg/s	5 deg/s
Maximum long. control rate $\dot{\varepsilon}_{\max}$	20%/s	10%/s
Bank time constant τ_σ	1.0	2.0
Long. control time constant τ_ε	0.8	2.0

disturbance, and if the tracking error exceeds the specified threshold, a new trajectory will be generated.

The initial altitude is fixed to 600 m for parafoil 1 and 1200 m for parafoil 2 for all simulations. The initial position is uniformly dispersed within a 800 m square centered on the position of the target in the wind-fixed coordinate frame in which the a priori wind profile is used to calculate the position in the wind-fixed frame. The initial heading is uniformly dispersed between 0 and 2π. This gives an altitude margin range of 0.9 to 5.0 for parafoil 1 and 0.8 to 2.5 for parafoil 2. This represents a low-to-moderate range of altitude margin.

The terminal portion of a typical closed-loop trajectory for parafoil 1 in the presence of wind uncertainty is shown in Fig. 9. In this case, only lateral control was used. The dark arrows indicate the true wind velocity and direction, and the light arrows indicate the expected wind velocity and direction from the a priori wind profile. In this case, the true wind velocity is nearly half of the expected value for most of the trajectory. The closed-loop guidance was able to overcome the wind uncertainty, and the final miss distance was 12 m.

Figure 10 presents the results from 100 simulated drops of parafoil 1 that have perfect knowledge of the wind profile ($\tilde{\mathbf{W}}(\tau) = 0$). In the simulations, navigation errors/uncertainty with statistics given in Table 3 are added that are unknown to the guidance and control. These errors correspond to a typical low-cost commercially available Global Positioning System (GPS) and barometric-altimeter-based inertial measurement unit (IMU). The position and altitude error models include a time-varying bias and noise. For each of the dispersed cases, the simulation is performed with both longitudinal and cross-track control and with only cross-track control, respectively. The radii of the inner and outer dashed circles are equal to the minimum turn radius of the system and twice the minimum turn radius of the system, respectively. It is illustrative to compare the landing position with the system turn radius, as this gives reference to the maneuverability of the system. The average and maximum miss distances for this case are 1.8 and 4.5 m for the system with both longitudinal and lateral control and 2.2 and 10.4 m for the system with only lateral control. We see that for both systems, all landings occur well within one minimum turn radius and that the landing errors are larger in the downrange direction, with the effect more pronounced for the system without longitudinal control. The elongation is primarily due to errors in the measured altitude, as every meter of altitude measurement error corresponds to approximately 2 m of landing error in the absence of wind and at nominal $\varepsilon = 0$.

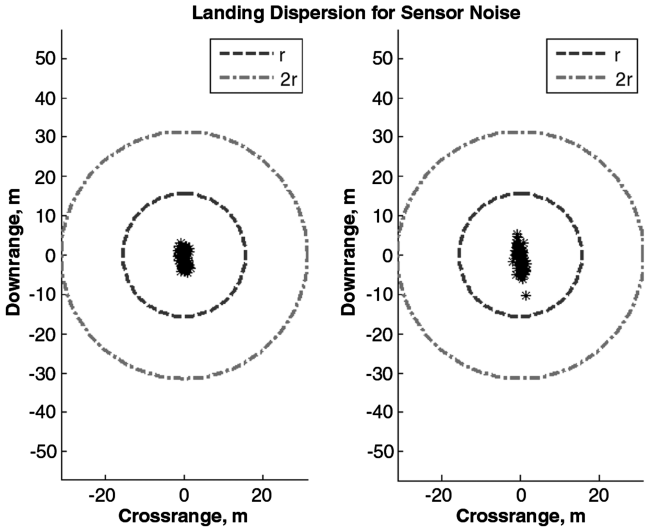

Fig. 10 Landing dispersion results for parafoil 1 for the case in which the wind profile is perfectly known and navigation errors are present: system with longitudinal and lateral control (left) and system with lateral control only (right).

Figure 11 presents the results from 100 simulated drops of parafoil 1 with uncertainty in the payload mass, which leads to errors in the wing loading and thus the glide speed. The uncertainty for each run is modeled as

$$m = m_{\text{nom}}(1 + \delta) \tag{105}$$

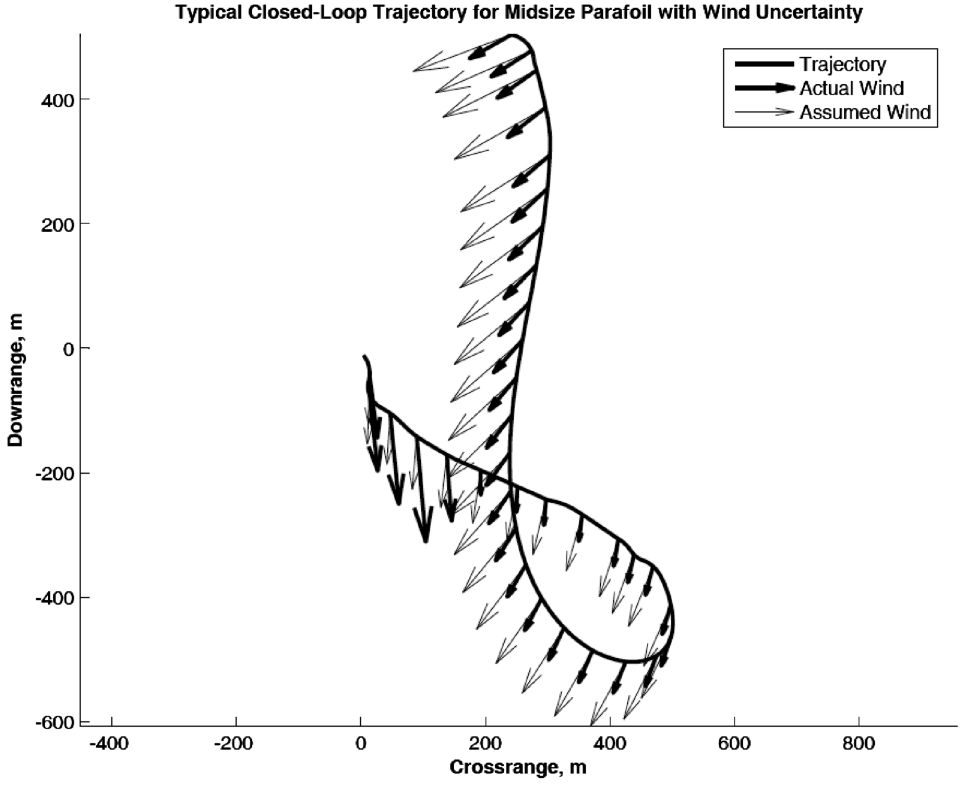

Fig. 9 This is the terminal phase of a typical closed-loop trajectory for parafoil 1 in the presence of wind uncertainty. Observe that the true wind velocity magnitude (dark) is nearly half of the expected value (light) for most of the trajectory.

Table 3 Sensor error statistics corresponding to a low-cost commercially available GPS and barometric-pressure-aided IMU

Position error	<1 m, time-correlated
Altitude error	<1.7 m, time-correlated
Compass bias	2 deg (1σ)
Compass noise	2 deg (1σ)

where m_{nom} is the expected mass value and δ is a zero-mean Gaussian variable with standard deviation $\sigma = 0.1$. Uncertainty in the glide airspeed introduces errors into the estimation of position in the wind-fixed coordinate frame [see Eqs. (30) and (31)] and errors in the modeled turn rate for a given flap deflection. The average and maximum miss distances are 0.6 and 22.9 m for the system with both longitudinal and lateral control and 4.3 and 26.2 m for the system with only lateral control. We see that the system with both control channels is largely insensitive to variations in mass, whereas the system with only lateral control has a slight degradation in landing accuracy, although 98 of cases still land within one turn radius of the target. The single outlier in the plot for the system with longitudinal control corresponds to a case in which the mass is significantly less than the expected mass and the wind is largely biased along the negative downrange axis. With the resulting lower airspeed, the system is blown further downwind than expected, to the point at which the longitudinal control authority can no longer compensate within the remaining altitude.

Figure 12 presents the results from 100 simulated drops of parafoil 1 with uncertainty in the expected C_L and C_D, which leads to errors in both the glide-path angle and glide airspeed. The uncertainty for each run is modeled as

$$C_L = C_{L_{\text{nom}}}(1 + \delta_1) \qquad C_D = C_{D_{\text{nom}}}(1 + \delta_2) \tag{106}$$

where δ_1 and δ_2 are independent zero-mean Gaussian variables with standard deviation $\sigma = 0.05$. This represents a moderate variation from the expected canopy performance. The average and maximum miss distances are 0.7 and 2.5 m for the system with both longitudinal and lateral control, and 14.6 and 75.2 m for the system with only lateral control. We see that the system with both longitudinal and lateral control is able to compensate for the performance variation, with all cases landing well within one minimum turn radii. The system with only lateral control is much more sensitive to variations in canopy performance, as 21 cases land outside of the one-minimum-turn-radius circle and 9 land outside of the two-minimum-turn-radii circle. In all of the latter cases, the ratio L/D is much lower than the expected value. Thus, trajectory planning in the early portion of the trajectory assumes the maneuvering energy to be larger than it actually is, and at some point along the trajectory, the true altitude margin becomes negative and it is no longer possible to reach the target.

Figure 13 presents the results from 100 simulated drops of parafoil 1 with uncertainty in the wind profile. The magnitude and direction of the uncertainty are modeled as a random walk and the magnitude is bounded such that

$$|\bar{\mathbf{W}}(\tau)| \leq 0.2V_0 \tag{107}$$

This represents a small-to-modest uncertainty in the wind profile. The average and maximum miss distances are 0.88 and 3.45 m for the system with both longitudinal and lateral control, and 8.0 and 51.5 m for the system with only lateral control. We see that the system with longitudinal and lateral control is able to compensate for the wind

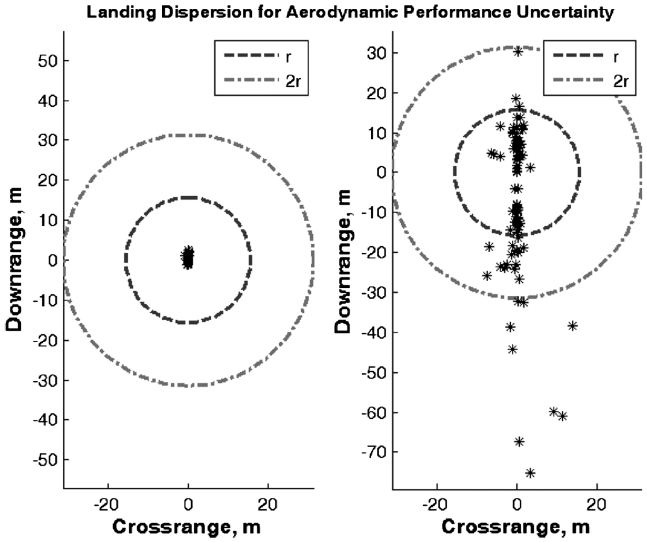

Fig. 12 Landing dispersion results for parafoil 1 for the case in which the wind profile is perfectly known and the C_L and C_D are varied ±5% (1σ) from the nominal values: system with longitudinal and lateral control (left) and system with lateral control only (right).

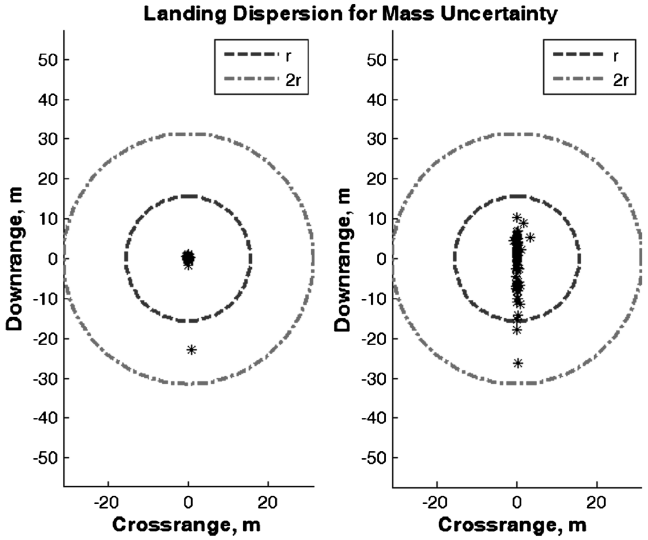

Fig. 11 Landing dispersion results for parafoil 1 for the case in which the wind profile is perfectly known and the payload mass is varied ±10% (1σ) from the nominal value: system with longitudinal and lateral control (left) and system with lateral control only (right).

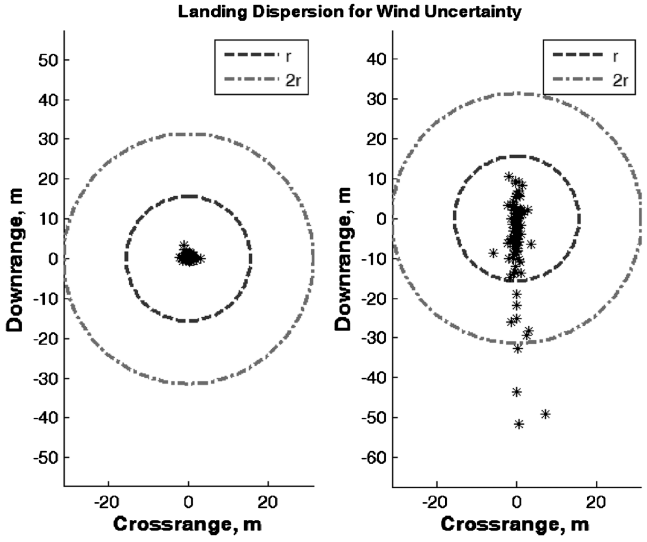

Fig. 13 Landing dispersion results for parafoil 1 for the case in which there wind profile magnitude is in error by 20% of the nominal vehicle airspeed and the direction varies from 0 to 360 deg: system with longitudinal and lateral control (left) and system with lateral control only (right).

uncertainty, with all of the cases landing within one minimum turn radius. The system with only lateral control, as before, is more sensitive to errors in the a priori wind profile, with 10 cases landing outside of one minimum turn radius and 4 cases outside of two minimum turn radii. The reason is due primarily to errors in estimating position in the wind-fixed coordinate frame early in the trajectory causing the true altitude margin (based off the actual wind profile) to go negative and the inability to decrease the along-track trajectory error later in the trajectory. These results illustrate the importance of obtaining the best possible a priori wind data.

Figure 14 presents the results from 100 simulated drops for parafoil 1 with all dispersions active, including sensor noise, mass, C_L and C_D, and wind uncertainty, all as described previously. The average and maximum miss distances are 2.0 and 5.8 m for the system with both longitudinal and lateral control, and 18.8 and 206 m for the system with only lateral control. The system with longitudinal control again has all of the cases landing within the minimum-turn-radius circle. This shows that, overall, the system with longitudinal control is robust to sensor noise, parameter uncertainty, and wind variation. The system with only lateral control has 30 cases landing outside the minimum-turn-radius circle and 17 cases landing outside the two-turn-radii circle. As with previous cases, uncertainty in system parameters and the a priori wind profile lead to errors in estimating position in the wind-fixed coordinate frame that, coupled with the inability to reduce along-track error, lead to a larger landing dispersion.

Figure 15 presents the results from 100 simulated drops for parafoil 2 with all dispersions active, including sensor noise, mass, C_L and C_D, and wind uncertainty, all as described previously. The average and maximum miss distances are 12.5 and 351 m for the system with both longitudinal and lateral control, and 51.1 and 557 m for the system with only lateral control. As with the smaller parafoil, we see that the system with longitudinal control is largely robust to uncertainty in parameters and the wind profile. There are two cases that land outside the minimum-turn-radius circle and one outside of the two-turn-radii circle. These are cases in which the wind uncertainty is largely biased along the negative x axis and the canopy performance is significantly less than expected. The system with lateral control only has 10 cases outside the minimum-turn-radius circle and 2 outside of the two-turn-radii circle. As compared with the results for parafoil 1, we see that parafoil 2 generally has a smaller landing dispersion pattern compared with its minimum turn radius for both cases with and without longitudinal control. This is largely due to the larger nominal airspeed for parafoil 2 that reduces errors in estimating position in the wind-fixed coordinate and decreases sensitivity to unknown variations in the wind.

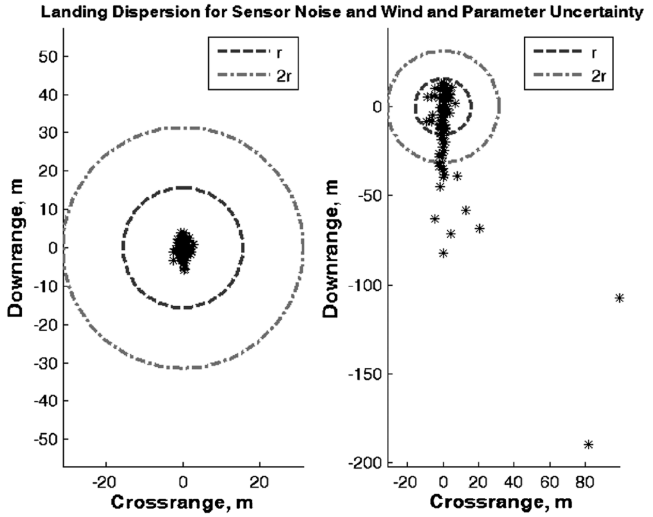

Fig. 14 Landing dispersion results for parafoil 1 for the case including navigation errors, wind uncertainty, and variations in aerodynamic performance and payload massv.

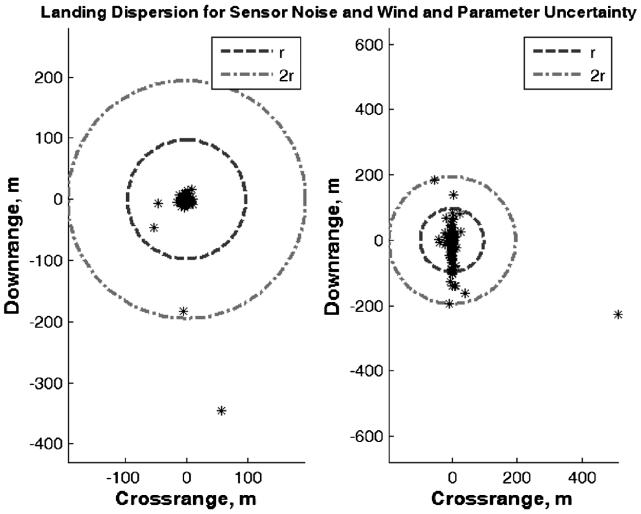

Fig. 15 Landing dispersion results for parafoil 2 for the case including navigation errors, wind uncertainty, and variations in aerodynamic performance and payload mass: system with longitudinal and lateral control (left) and system with lateral control only (right).

VII. Conclusions

This paper presents an advanced parafoil guidance algorithm for cases in which it is desired to fix the final azimuth upon landing. The foundation of the algorithm is a fixed-time trajectory planner that generates one of two types of trajectories, both with a fixed final heading, based on the position relative to the target and known information on the wind profile and parafoil canopy performance. The planning algorithm uses a low-fidelity model that requires only three parameters that adequately summarize the behavior of the system and are readily available for a given canopy and payload weight. In this way, the guidance is fully parameterized on known information about the system and is readily adapted to different canopies and/or payloads. The guidance algorithm has the potential to be applied to a broad class of autonomous parafoils that encompass gross variations in the lift-to-drag ratio, wing loading, and maximum turn rate.

The algorithm was demonstrated for two different classes of parafoil systems, one a typical small- to midscale canopy with light loading and the other a typical large-scale system with high loading. Cases were run for both systems using lateral control only and lateral plus longitudinal control. It was shown that the system with longitudinal control was robust to variations from expected system parameters and wind profile uncertainty, a trend previously shown in [9]. It was also shown that systems with lateral control only are more sensitive to both wind profile and parameter uncertainty, with the strongest sensitivity being to uncertainty in the system lift-to-drag ratio L/D and wind profile uncertainty.

Acknowledgments

The authors at Iowa State University acknowledge the support to this work by NASA grants NNJ05JG70H, NNJ06JI04H, and NNX07AV10H.

References

[1] Calise, A. J., and Preston, D., "Swarming/Flocking and Collision Avoidance for Mass Airdrop of Autonomous Guided Parafoils," *Journal of Guidance, Control, and Dynamics*, Vol. 31, No. 4, 2008, pp. 1123–1132. doi:10.2514/1.28586

[2] Tavan, S., "Status and Context of High Altitude Precision Aerial Delivery Systems," AIAA Paper 2006-6793, Aug. 2006.

[3] Jann, T., "Advanced Features for Autonomous Parafoil Guidance, Navigation, and Control," *Journal of Guidance, Control, and Dynamics*, Vol. 31, No. 4, 2008, pp. 1123–1132. doi:10.2514/1.28586

[4] Rademacher, B. J., "Minimum Complexity Guidance, Navigation, and Control for an Autonomous Parafoil Payload Delivery System," M.S. Thesis, Iowa State Univ., Ames, IA, 2005.

[5] Soppa, U., Görlach, T., and Roenneke, A. J., "German Contribution to the X-38 CRV Demonstrator in the Field of Guidance, Navigation, and Control (GNC)," *Acta Astronautica*, Vol. 56, No. 8, 2005, pp. 737–749. doi:10.1016/j.actaastro.2004.11.010

[6] Kaminer, I. I., and Yakimenko, O. A., "Development of Control Algorithm for the Autonomous Gliding Delivery System," AIAA Paper 2003-2116, May 2003.

[7] Gimadieva, T. Z., "Optimal Control of a Gliding Parachute System," *Journal of Mathematical Sciences*, Vol. 103, No. 1, 2001, pp. 54–60. doi:10.1023/A:1026626528909

[8] Hattis, P. D., Campbell, D. P., Carter, D. W., and McConley, M., "Providing Means for Precision Airdrop Delivery from High Altitude," AIAA Paper 2006-6790, Aug. 2006.

[9] Slegers, N., Beyer, E., and Costello, M., "Use of Variable Incidence Angle for Glide Slope Control of Autonomous Parafoils," *Journal of Guidance, Control, and Dynamics*, Vol. 31, No. 3, 2008, pp. 585–596. doi:10.2514/1.32099

[10] Dubins, L. E., "On Curves of Minimal Length with a Constraint on Average Curvature and with Prescribed Initial and Terminal Positions and Tangents," *American Journal of Mathematics*, Vol. 79, No. 3, 1957, pp. 497–516. doi:10.2307/2372560

[11] Boissonnat, J. D., Cérézo, A., and Leblond, J., "Shortest Paths of Bounded Curvature in the Plane," *Proceedings of the 1992 IEEE International Conference on Robotics and Automation*, Inst. of Electrical and Electronics Engineers, Piscataway, NJ, 1992.

[12] McGee, T. G., Spry, S., and Hedrick, J. K., "Optimal Path Planning In a Constant Wind With a Bounded Turning Rate," AIAA Paper 2005-6186, Aug. 2005.

[13] McNeely, R., Iyer, R., and Chandler, P., "Tour Planning for an Unmanned Air Vehicle Under Wind Conditions," *Journal of Guidance, Control, and Dynamics*, Vol. 30, No. 5, 2007, pp. 1299–1306. doi:10.2514/1.26055

[14] Larson, R. A., Pachter, M., and Mears, M. J., "Path Planning by Unmanned Air Vehicles for Engaging and Integrated Radar Network," AIAA Paper 2005-6191, Aug. 2005.

[15] Sussmann, H. J., "Shortest 3-Dimensional Paths with a Prescribed Curvature Bound," *Proceedings of the 34th Conference on Decision and Control*, Inst. of Electrical and Electronics Engineers, Piscataway, NJ, 1995, pp. 3306–3312. doi:10.1109/CDC.1995.478997

[16] Liang, T. C., Liu, J. S., Hung, G. T., and Chang, Y. Z., "Practical and Flexible Path Planning for Car-Like Mobile Robot Using Maximal-Curvature Cubic Spiral," *Robotics and Autonomous Systems*, Vol. 52, No. 4, 2005, pp. 312–335. doi:10.1016/j.robot.2005.05.001

[17] Moll, M., and Kavraki, L. E., "Path Planning for Minimal Energy Curves of Constant Length," *Proceedings of the 2004 IEEE International Conference on Robotics and Automation*, Inst. of Electrical and Electronics Engineers, Piscataway, NJ, May 2004, pp. 2826–2831. doi:10.1109/ROBOT.2004.1307489

[18] Lu, P., and Chavez, F. R., "Nonlinear Optimal Guidance," AIAA Paper 2006-6087, August 2006.

[19] Thomasson, P. G., "Equations of Motion of a Vehicle in a Moving Fluid," *Journal of Aircraft*, Vol. 37, No. 4, 2000, pp. 630–639. doi:10.2514/2.2645

[20] Barrows, T. M., "Apparent Mass of Parafoils with Spanwise Camber," *Journal of Aircraft*, Vol. 39, No. 3, 2002, pp. 445–451. doi:10.2514/2.2949

[21] Brown, G. J., "Parafoil Steady Turn Response to Control Input," AIAA Paper 1993-1241, May 1993.

[22] Lingard, J. S., "The Performance and Design of Ram-Air Gliding Parachutes," Royal Aircraft Establishment, TR 81103, London, 1981.

[23] Iacomini, C. S., and Cerimele, C. J., "Longitudinal Aerodynamics From A Large-Scale Parafoil Test Program," AIAA Paper 1999-1732, June 1999.

[24] Iacomini, C. S., and Madsen, C. M., "Investigation of Large Scale Parafoil Rigging Angles: Analytical and Drop Test Results," AIAA Paper 1999-1752, June 1999.

[25] Jardin, M. R., and Erzberger, H., "Atmospheric Data Acquisition and Interpolation for Enhanced Trajectory-Prediction Accuracy in the Center-TRACON Automation System," AIAA Paper 1996-271, Jan. 1996.

[26] Kelly, K., and Peña, B., "Wind Study and GPS Dropsonde Applicability to Airdrop Testing," AIAA Paper 2001-2022, May 2001.

[27] Lee, E. B., and Markus, L., *Foundations of Optimal Control Theory*, Wiley, New York, 1967, pp. 259–265.

[28] Shkel, A. M., and Lumelsky, V., "Classification of the Dubins Set," *Robotics and Autonomous Systems*, Vol. 34, No. 4, 2001, pp. 179–202. doi:10.1016/S0921-8890(00)00127-5

[29] *Atmospheric Soundings* [online database], Univ. of Wyoming, Dept. of Atmospheric Science, http://weather.uwyo.edu/upperair/sounding.html [retrieved 3 July 2008].